

Sedimentation and fluttering of a cylinder in a confined liquid

Maria Veronica D'Angelo* and Mario Cachile†

*Universidad de Buenos-Aires, Facultad de Ingeniería, GMP-LIA-FMF, CONICET,
Paseo Colón 850, 1063, Buenos Aires, Argentina*

Jean-Pierre Hulin‡ and Harold Auradou§

*Laboratoire FAST, Univ. Paris Sud, CNRS, Université Paris-Saclay, F-91405, Orsay, France
(Received 22 November 2016; published 5 October 2017)*

The sedimentation and fluttering (angular oscillation of the axis) of straight cylinders are studied in a viscous fluid at rest filling a vertical Hele-Shaw cell for different density contrasts $\rho_s - \rho_f$ and fluid viscosities μ_f and for two cylinder densities ρ_s and diameters D . The influence of confinement in the cell is studied by comparing the present results to those of the literature for nonconfined fluids. While the confinement and the cylinder length L both influence strongly the mean sedimentation velocity V_s , the characteristics of the fluttering instability are much more similar in the confined and nonconfined cases. While the drag coefficient is nearly constant in a nonconfined fluid, it is larger here and depends both on L (due to flow blockage) and on the Reynolds number $\text{Re}_D = V_s D \rho_f / \mu_f$; the inertial and viscous drag components have equal magnitudes for $\text{Re}_D \simeq 40$. For fluttering, instead, the key parameter is the Froude number $\text{Fr} = V_s / V_g$ [$V_g = \sqrt{(\rho_s - \rho_f)gL / \rho_f}$], and the fluttering oscillations vanish below $\text{Fr} \sim 0.07$ for all cylinders and fluids investigated. Above this threshold, the angular amplitude increases with Fr up to a plateau value, while that of the horizontal oscillations is, at first, very large and then decreases; both amplitudes are reduced when the viscous drag is dominant, but, if inertial drag is dominant, all data points follow a common trend. For all fluids and cylinders, too, the fluttering frequency varies as $f = 0.102 V_g / L$. These features of fluttering are generally qualitatively similar to those reported in nonconfined fluids, but this instability is observable down to lower Re_D values ($\simeq 24$ instead of ~ 200).

DOI: [10.1103/PhysRevFluids.2.104301](https://doi.org/10.1103/PhysRevFluids.2.104301)

I. INTRODUCTION

The dynamics of objects with a large aspect ratio sedimenting freely in a fluid is a classical problem in hydrodynamics and aerodynamics, the analysis of which goes back to such authors as Maxwell [1] or Kirchhoff [2]. Depending on the physical control parameters and the initial conditions [3], the stationary vertical sedimentation motion may be combined to time-dependent horizontal displacements and to variations of the angle with respect to the horizontal [4] which can be periodic or chaotic (flutter) [5,6], or to periodic or chaotic tumbling in which the object rotates about its center of mass [7–11]. Many studies of such phenomena have been performed in order to identify the different flow regimes and the relevant dimensionless numbers determining the transition between them.

A particularly interesting case is that of confined configurations in which the diameter of the falling solid objects is a large fraction of the distance between the channel walls: this strong local obstruction by the object creates large back-flow and fluid entrainment effects which perturb

*vdangelo@fi.uba.ar

†mcachil@fi.uba.ar

‡hulin@fast.u-psud.fr

§auradou@fast.u-psud.fr

considerably its motion. Practically, this corresponds to the transport of particles in such media as fractured rocks, frequently encountered in the petroleum and gas engineering industries and in geothermal reservoirs. These flow configurations are also encountered in chemical reactors with plane walls or in plate heat exchangers. Confinement limits three-dimensional (3D) effects and allows therefore for two-dimensional (2D) numerical simulations. Experimentally, it also makes possible a precise quantitative determination of the trajectory of the objects. Belmonte [4] used, for instance, thin rectangular sheets perpendicular to parallel side walls and of width very close to the distance between the latter. Moreover, confinement often modifies the relative magnitude of the viscous and inertial forces and influences the dynamics of the falling objects and the onset of the instabilities.

The present work is therefore centered on the influence of confinement on the fluttering motion of cylinders of large aspect ratios sedimenting between vertical parallel walls (Hele-Shaw cell geometry); a strong confinement is obtained by using cylinder diameters which correspond to 0.68 times and 0.79 times the spacing between the walls. The cylinders mimic the fibers used in hydraulic fracturing [12,13] for recovering oil and/or gas from tight low-porosity reservoirs or for circulating water in hot dry rocks for geothermal steam generation.

In a nonconfined case, the phenomenon is controlled by five independent variables [6] (two for the geometry of the object, its density and the fluid density and viscosity) from which three dimensionless numbers can be constructed [3]: the dimensionless moment of inertia, the aspect ratio of the object, and the Reynolds number. When the influence of inertia is low (e.g., a flattened object falling vertically) and for small Reynolds numbers, the motion is overdamped and the object falls without any oscillation. If the dimensionless moment of inertia is increased (e.g., a more spherical particle), one observes frequently a tumbling motion. Finally, for small moments of inertia, and Reynolds number above 100, both the orientation of the cylinder and the coordinates of its center of gravity oscillate periodically. In a pioneering work, Marchildon *et al.* [14] analyzed the motion of (~ 100) cylinders of different materials and dimensions: they obtained a scaling relation satisfied by the frequency of their oscillations. Chow and Adams [15] also compared satisfactorily to these predictions the frequency of the oscillations of straight and curved cylinders sedimenting in a large container (see Sec. IV).

In previous works [16,17], we had already investigated the stability of the motion of similar cylinders in Hele-Shaw cells for a broader range of values of the confinement ratio D/H and with both a nonzero and a zero mean flow inside the cell. (D is the diameter of the cylinders and H the distance of the cell walls.) At values of D/H between 0.4 and 0.55 the cylinders oscillate perpendicular to the flow and to the front walls of the cell and display a rolling motion about their main axis but remain horizontal [16,18,19]. The detailed characteristics of these transverse oscillations and, particularly, the influence of the mean flow are reported in detail in Ref. [17]. For $D/H \gtrsim 0.55$, an additional fluttering motion is superimposed onto the transverse one and induces oscillations of both the angle of the axis of the cylinder with respect to the horizontal and of the horizontal coordinate of its center of mass. For $D/H \gtrsim 0.6$, the transverse oscillation disappears, and only the fluttering instability is observed. In the context of fiber transport in fractures, the displacements induced by these latter oscillations may have a strong influence by introducing interactions between the fibers: the amplitude and frequency of the oscillations provide crucial information on the volume explored by the fibers and, therefore, on their interactions.

For the values 0.68 and 0.79 of D/H in the present experiments, only the fluttering instability is present. Moreover, in order to simplify further the configuration of the flow and the analysis of the results, no mean flow is applied and the cylinders move solely under the influence of gravity. The whole trajectory of all the falling cylinders is analyzed as a function of time in order to determine the mean sedimentation velocity and the frequency and amplitudes of the oscillations. The analysis of the variation of these variables with the length L and density ρ_s of the cylinders and the properties of the fluid (viscosity μ_f , density ρ_f) has been performed for a broad range of values of these parameters and compared to those reported by other authors for similar sedimentation experiments

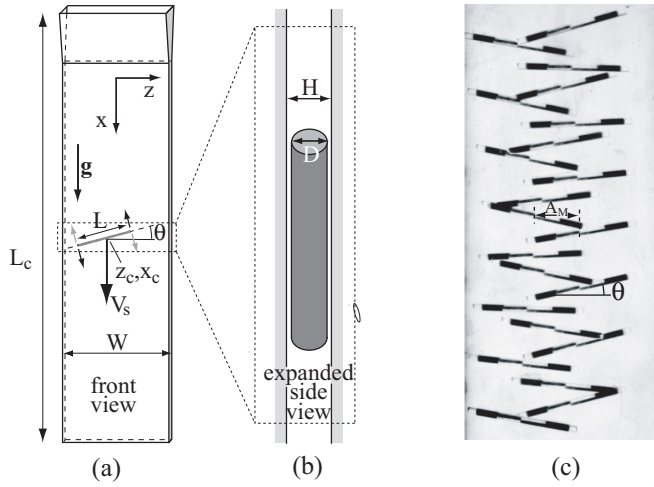


FIG. 1. (a) Schematic front view of the experimental setup; oblique gray and black arrows represent the motion corresponding to the fluttering oscillations. $L_c = 400$ mm, $W = 90$ mm. (b) Expanded side view of the slice of the aperture containing the cylinder (dotted rectangle in panel a). $H = 2.8$ mm. (c) Sequences of views taken at constant time intervals in the fluttering regime (the cylinder moves downward). $L/W = 0.49$, $D/H = 0.79$, $U = 7.15$ mm s⁻¹ (*WG10* solution), $\Delta t = 0.66$ s, field of view: 78×167 mm.

performed in a nonconfined fluid. This comparison will show that the influences of confinement on the mean sedimentation motion and on the fluttering process are very different.

II. EXPERIMENTAL SETUP AND PROCEDURE

The cylinders sediment inside a liquid filled rectangular plexiglass cell of width $W = 90$ mm, length $L_c = 400$ mm, and distance $H = 2.8$ mm between the largest walls (Fig. 1). Schematic views of the experimental setup and a typical sequence of pictures of a cylinder falling in the fluttering regime are shown in Fig. 1. One cylinder at a time is released at the top of the container below the fluid surface. The first 50 mm of the container have a Y-shape, and the aperture decreases continuously with the downward distance from 10 mm to H . This ensures well-controlled initial conditions and reproducible measurement results.

Two different kinds of cylinders have been used: one type is made of plexiglas (PMMA) of density $\rho_s = 1.19$ g cm⁻³ and has a diameter $D = 2.2$ mm ($D/H = 0.79$), and the second type is made of carbon fibers of higher density $\rho_s = 1.54$ g cm⁻³ and its diameter is $D = 1.9$ mm ($D/H = 0.68$). The length L of the cylinders ranged between 5 and 45 mm for most experiments. As mentioned above, in both cases, the ratio D/H is large enough so that no transverse oscillations of the cylinder occur [17]. Then, from Refs. [16,19], the cylinder remains in the middle plane between the cell walls and does not interact with them.

The liquids used in the experiments are either pure water or water-glycerol solutions (relative glycerol concentrations in weight $5 \leq c \leq 30$ %). The physical parameters characterizing these solutions are listed in Table I.

The motion of the cylinders is monitored by a digital camera with a spatial resolution of 0.13 mm/pixel and a frame size of 504×1584 pixels. The images are acquired at constant intervals (1/60 s): all images are processed after each experiment in order to determine the instantaneous position of the center of mass [coordinates $x_c(t)$ and $z_c(t)$] and the corresponding tilt angle $\theta(t)$ of the cylinder axis with respect to the horizontal. The variations of both z_c and θ with time are generally well fitted by a sine-wave variation which provides the frequency f , the amplitudes, and the relative phase of their respective oscillations. The time variation of the vertical coordinate x_c of

TABLE I. Physical properties of the solutions used in the experiments at a temperature $T = 25$ °C. Mass concentration of glycerol: c ; density: ρ_f ; dynamical viscosity: μ_f . The symbols at right are those used in the graphs: open symbols correspond to PMMA cylinders and black symbols to the carbon ones.

Name	c (%)	ρ_f (g/cm ³)	μ_f (mPa s)	μ_f/μ_{water}	Symbols
	Water and water-glycerol solutions				
W	0	0.997	0.89	1	$\nabla, \blacktriangledown$
$WG5$	5	1.008	1.01	1.13	\triangle
$WG10$	10	1.02	1.15	1.29	\circ, \bullet
$WG15$	15	1.032	1.33	1.49	\diamond
$WG20$	20	1.044	1.542	1.73	\square, \blacksquare
$WG30$	30	1.075	2.1	2.36	$\triangleleft, \blacktriangleleft$

the center of mass corresponds to the superposition of a mean drift providing the constant global sedimentation velocity V_s and of vertical oscillations of frequency $2f$ [17].

For practical reasons, each cylinder is used only once. The repeatability of the measurement is tested by performing two to four experiments using cylinders of lengths differing by, at most, 2%. The values of the frequency f and the mean velocity V_s used in the plots are obtained by averaging the results of these different experiments: individual values differ by less than $\pm 2\%$ from the mean one.

Narrow stripes have been painted on the cylinder and parallel to its axis in order to detect indirectly displacements of the cylinder away from the midplane of the cell: the latter induce rotations of the cylinder due to the velocity gradients of the Poiseuille profile. These rotations are detected from the relative motion of the stripes and the cylinder axis [16]: no such displacements were present in the experiments performed in the present work as expected for the high values of the ratio D/H which have been used [17].

III. MEAN VERTICAL SEDIMENTATION VELOCITY

We discuss now the variation of the time average of the vertical component of the sedimentation velocity V_s with the density and length of the cylinders and with the density and viscosity of the fluid. These data allow us to determine both the viscous and inertial drag forces on the cylinder and the dependence of their ratio on the Reynolds number: the influence of confinement inside the Hele-Shaw cell is evaluated by comparing these results to those reported for nonconfined fluids.

The sedimentation velocities measured experimentally are plotted in Fig. 2 for both PMMA and carbon cylinders as a function of their length L : this plot contains data corresponding both to the stationary and to the fluttering regimes but no abrupt variation of V_s is observed at the transition between them. The velocity decreases monotonically by a factor (1.5–2) as L increases in agreement with our previous studies using a similar confined geometry both with and without an imposed flow (Fig. 4 in Ref. [17]). This behavior contrasts strongly with that found in the absence of confinement [20,21]: in this latter case, the velocity slowly increases with the length of the cylinders and finally tends towards a constant.

As could be expected, for a given water-glycerol solution, V_s is significantly larger for carbon cylinders than for PMMA ones (by a factor of 2–3) due to their larger density contrast with the fluid. For a given cylinder, the velocity is lower for the water-glycerol solutions of higher concentration: in this case, both the reduced density contrast and the increased viscosity contribute to this variation.

These results allow us to estimate now the forces acting on the cylinder. In the constant sedimentation velocity regime, the weight of the cylinder, corrected from the effect of buoyancy ($M'g$), is balanced by an hydrodynamic vertical drag force F_x with $M'g + F_x = 0$. The force F_x includes an inertial (F_{xi}) and a viscous (F_{xv}) component. Using classical definitions, F_{xi} can be

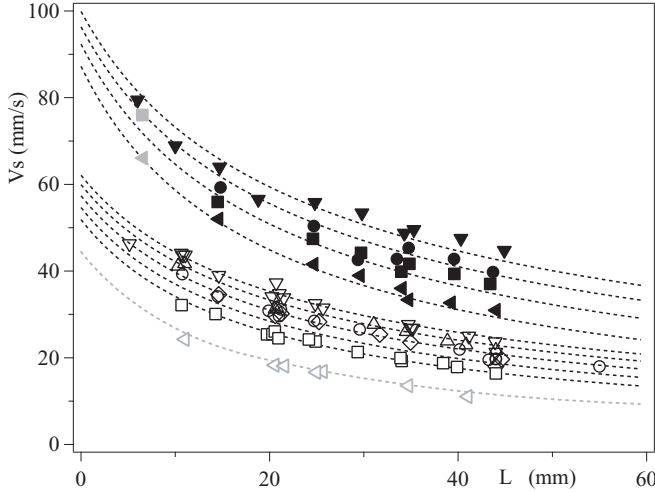


FIG. 2. Variation of the mean vertical downward sedimentation velocity V_s as a function of the length L for PMMA (open symbols) and carbon (dark symbols) cylinders in water-glycerol solutions of different mass concentrations c of glycerol. Pure water ($\nabla, \blacktriangledown$); water-glycerol solutions: $c = 5\%$ (Δ, \bullet), $c = 10\%$ (\circ, \bullet), $c = 15\%$ (\diamond), $c = 20\%$ (\square, \blacksquare), $c = 30\%$ ($\triangleleft, \blacktriangleleft$). Gray symbols correspond to experiments for which no oscillations were observed. Dotted lines: theoretical variations $V_s(L)$ obtained by solving the implicit Eq. (8).

written as

$$F_{xi} = \frac{1}{2}\rho_f C_{di} DL V_s^2, \quad (1)$$

where DL is the area of the object projected on a plane normal to the flow and C_{di} is the drag coefficient for purely inertial forces. Assuming, as is often the case at low Reynolds numbers, that L is the most relevant characteristic length for the viscous forces leads to [20]

$$F_{xv} = \mu_f C_{dv} L V_s. \quad (2)$$

The force balance equation becomes then, since $M'g = \pi(\rho_s - \rho_f)gL D^2/4$,

$$\frac{\pi}{4}(\rho_s - \rho_f)gL D^2 = \frac{1}{2}\rho_f C_{di} DL V_s^2 + \mu_f C_{dv} L V_s = \frac{1}{2}\rho_f C_d DL V_s^2. \quad (3)$$

The expression after the first equal sign is a second order development describing the transition between viscous drag ($\propto V_s$) at low Reynolds numbers [20,21] and inertial drag ($\propto V_s^2$) at high ones. Summing the two terms reflects the combination of these two force components at intermediate Reynolds numbers. The expression of the global drag component is then obtained by dividing the two terms of the last equality by $1/2 \rho_f DL V_s^2$:

$$C_d = C_{di} + \frac{2}{\text{Re}_D} C_{dv}. \quad (4)$$

Using the balance between the global drag and the buoyancy force, C_d is computed for each experiment from the experimental sedimentation velocity:

$$C_d = \frac{\pi}{2} \frac{(\rho_s - \rho_f) g D}{\rho_f V_s^2}. \quad (5)$$

Figure 3 displays the variations with Re_D of C_d computed from Eq. (5) for cylinders of different lengths (in the present experiments, $12 \leq C_d \leq 180$). Each set of points corresponding to a given length L follows a single common trend, although it includes data corresponding to both carbon and PMMA cylinders and to different fluid solutions: this suggests that C_d does not depend specifically

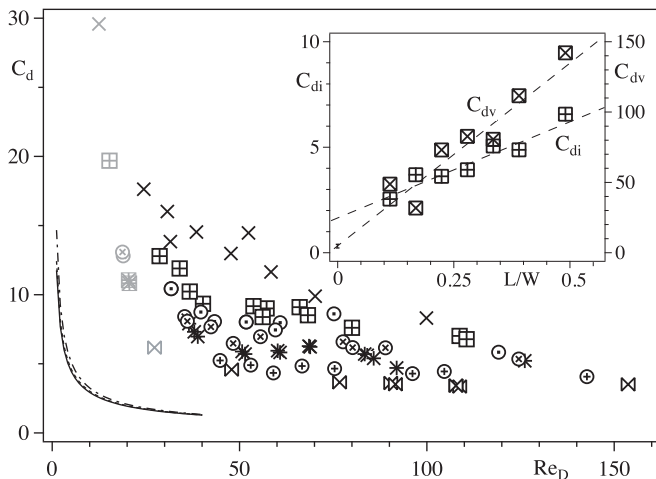


FIG. 3. Main graph: Variation of the global drag coefficient C_d as a function of the Reynolds number $Re_D = \rho_f V_s D / \mu_f$ for lengths L of the sedimenting cylinder: $L = 10$ mm (\triangleright), $L = 15$ mm (\oplus), $L = 20$ mm ($*$), $L = 25$ mm (\otimes), $L = 30$ mm (\odot), $L = 35$ mm ($+$), $L = 44$ mm (\times). Each symbol corresponds to both PMMA and carbon cylinders. Gray symbols: experiments with no oscillations. Curves at bottom left: predictions from Ref. [21] (table 7) for cylinders in an infinite fluid with $L/D = 22.5$ (continuous line), 12.5 (dotted), 5 (dashed-dotted). Insert: Variation with L/W of the coefficients C_{di} (\boxplus) and C_{dv} (\boxtimes) determined by fitting the data of the main graph using Eq. (4); dashed lines: variations corresponding to Eqs. (6). Vertical segment at bottom left ($L/W = 0$): range of theoretical values of C_{dv} for cylinders of same L and D values as here in a nonconfined fluid.

on ρ_s , ρ_f , or μ_f but rather on Re_D and on the ratio L/W characterizing the relative obstruction of the width of the cell by the cylinder. The influence of the dimensionless diameter D/H on fluttering is not studied here because its value was kept on purpose in the narrow range for which only fluttering appears; this influence was studied in a previous paper [17] and found to be weak. Overall, C_d decreases with Re_D and tends towards a constant asymptotic value which corresponds to the purely inertial component C_{di} . These variations have been compared to those obtained from the analytical expression given in Ref. [21]: these are shown in the range ($1 \leq Re_D \leq 40$) investigated in this reference for three values of L/D (22.5, 12.5, and 5) corresponding, in the present experiments, to lengths $L = 45$, 25, and 10 mm. One observes that the influence of the length L is much weaker than in the confined case and that the values of C_d are significantly lower at a given Reynolds number.

For each length L , C_{di} , and C_{dv} have been determined by performing a linear regression on the variations of C_d as a function of $1/Re_D$ in Fig. 3). The values obtained in this way are plotted in the insert of Fig. 3 as a function of the dimensionless ratio L/W . The variations of both C_{di} and C_{dv} with L/W are well fitted empirically within the experimental uncertainties by the following linear dependences:

$$C_{di} = (1.6 \pm 0.2) + (1.0 \pm 0.5)L/W, \quad (6a)$$

$$C_{dv} = (5 \pm 3) + (270 \pm 10)L/W. \quad (6b)$$

These increasing trends reflect the stronger perturbation of the flow by the cylinder (and the resulting larger drag) as L/W increases.

The constant term in Eqs. (6) corresponds to the limit $L/W = 0$, which is also the value for a nonconfined flow ($W \rightarrow \infty$). We have therefore compared it to the theoretical predictions of the force on a fixed cylinder in a uniform infinite flow [20,21]. Assuming that the angle between the

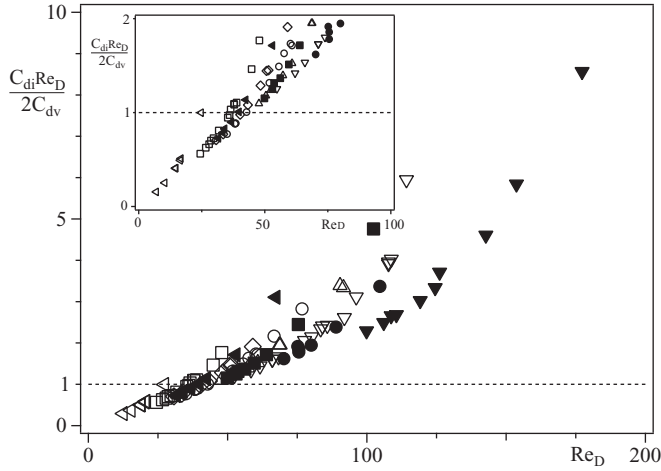


FIG. 4. Variation of the ratio $C_{di}Re_D/(2C_{dv})$ with the Reynolds number Re_D for the different cylinders and solutions used in the experiments (same symbols as in Fig. 2). Horizontal line: ratio equal to 1. Insert: expanded view of the region around $C_{di}Re_D/(2C_{dv}) = 1$.

flow and the normal to the cylinder is not too large, one obtains

$$C_{dv} = \frac{4\pi}{\ln(L/D) - 1/2}. \quad (7)$$

From this equation, C_{dv} varies slowly (logarithmically) with L/D and decreases only from 5.6 to 3.25 as L/D increases. This range of values (vertical bar on the axis $L/W = 0$) is compatible, within the experimental errors, with the corresponding experimental limit (5 ± 3) of C_{dv} for $L/W \rightarrow 0$.

The ratio $C_{di}Re_D/(2C_{dv})$ of the inertial and viscous drag components in Eq. (4), computed using Eqs. (6) is plotted in Fig. 4 as a function of the Reynolds number Re_D for all cylinders and solutions used in the experiments. Most data points follow a common linear increasing trend with upwards deviations for the shortest cylinders (for which the Reynolds number is largest). As could be expected, the ratio is largest (up to $\simeq 9$) for the shortest carbon cylinders in water and smallest (down to 0.3) for the longest PMMA cylinders in the most viscous solution. The two components are of the same order of magnitude for $Re_D \simeq 40$ (insert).

Combining the force balance relation (3) and Eq. (4) leads to the implicit equation (Re_D contains a factor V_s)

$$V_s = \sqrt{\frac{gD(\rho_s - \rho_f)}{\rho_f}} \sqrt{\frac{\pi}{2} \frac{1}{C_{di}(L) + 2C_{dv}(L)/Re_D}}. \quad (8)$$

By solving this equation iteratively (initializing with the value of V_s obtained by neglecting the viscous term) and using Eqs. (6), one obtains theoretical predictions for the variations of V_s with L . These predicted curves are shown as dotted lines in Fig. 2: they agree well with the experimental data (symbols) for all cylinders (carbon and PMMA) and solutions.

These measurements of the mean velocity of cylinders sedimenting in a confined Hele-Shaw cell geometry display therefore large differences with respect to similar ones performed in nonconfined geometries. More precisely, the velocity V_s decreases strongly, and the drag coefficient C_d increases when the length L increases, while, in nonconfined geometries, V_s and C_d vary only slowly with L and the value of C_d is lower. We compare now, for the same experiments, the variations of the angular and horizontal fluttering amplitudes motion and of its frequency to those reported for similar experiments in the nonconfined case.

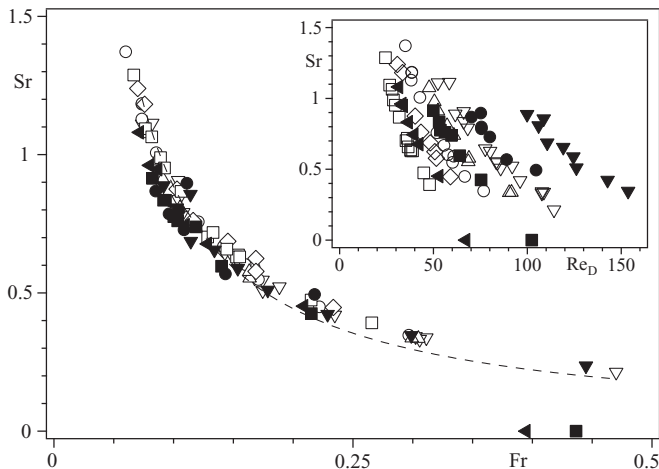


FIG. 5. Main graph: Variation of the Strouhal number ($Sr = fL/V_s$) with the Froude number ($Fr = V_s/V_g$). Dashed line: fit by $Sr \propto 1/Fr$. Insert: variation of Sr with the Reynolds number $Re_D = \rho_f V_s D / \mu_f$. Points with ($Sr = 0$) correspond to experiments for which no oscillations occurred. Experiments were realized using PMMA (open symbols) and carbon (dark symbols) cylinders sedimenting in pure water ($\nabla, \blacktriangledown$) and water-glycerol solutions of different mass concentrations: $c = 5\%$ (Δ), $c = 10\%$ (\circ, \bullet), $c = 15\%$ (\diamond), $c = 20\%$ (\square, \blacksquare), $c = 30\%$ ($\triangleleft, \blacktriangleleft$).

IV. FLUTTERING INSTABILITY

A. Fluttering frequency

In our experiments, the measured frequency of the fluttering oscillations ranges between 0.5 and 3 Hz. As usual in oscillatory hydrodynamic instabilities [10], we characterize this fluttering frequency by the dimensionless Strouhal number $Sr = fL/V_s$. The length L is chosen as the characteristic one for the instability because the latter involves flow variations over distances of the order of L ; this oscillating flow component cannot be considered as locally 2D like, for instance, the mean flow around the cylinder or that created by transverse oscillations [17]. This choice will be, in addition, justified *a posteriori* by the discussions below.

As a first step in the search of the relevant parameter controlling fluttering and by analogy with other periodic instabilities like vortex shedding, Sr is plotted as function of Re_D in the insert of Fig. 5 for different solutions and cylinders. Beyond the fact that, for a given cylinder and fluid, Sr decreases as Re_D increases, Sr cannot clearly be a function of Re_D only. Moreover, for the different cylinders and fluids, there is a significant dispersion of the threshold values of Re_D below which no oscillation occurs. We note, however, that, for the lightest and longest cylinders together with the more viscous fluids, oscillations are observed down to $Re_D = 24$ (the global range is $12 \leq Re_D \leq 180$); this is much lower than the threshold values ($Re_D \sim 200$) in nonconfined geometries [15]. For coherence, we plotted also (not shown in the figures): Sr as a function of a Reynolds number $Re_L = V_s \rho_f L / \mu_f$ based on the same characteristic length L as Sr (its range of values in the present experiments is $180 \lesssim Re_L \lesssim 2250$). The collapse of the different curves is not better than for Re_D , and neither Re_D nor Re_L nor, more generally, the relative influence of the viscous forces appear as the key parameters of the process.

No oscillations were observed ($Sr = 0$) for the two data points corresponding to the carbon cylinder in solutions $C = 20\%$ and $C = 30\%$ and to the highest values of Fr (~ 0.4 and ~ 0.43). This is unexpected since the corresponding Reynolds numbers are still rather large ($Re_D \sim 70$ and ~ 100), while the high Fr value should promote large oscillation amplitudes (Fig. 7). Due to the corresponding large values of V_s (upper gray symbols in Fig. 2), this likely means that the oscillations of the cylinder do exist but lack time to develop during the transit through the field of

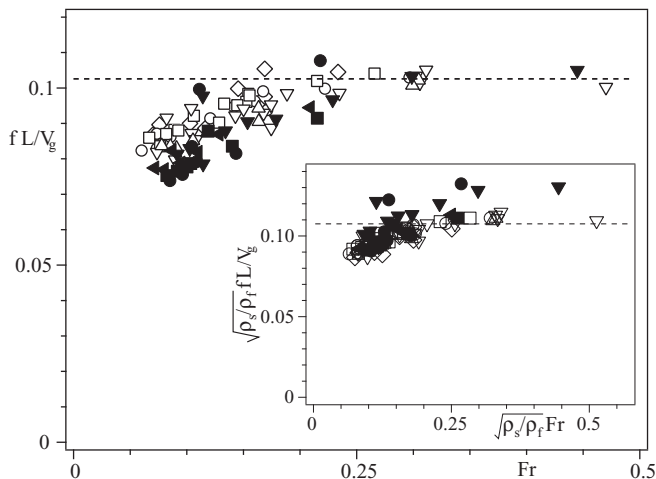


FIG. 6. Main graph: Variation of the dimensionless frequency of the angular oscillations $fL/V_g = \text{Sr Fr}$ with the Froude number; dashed horizontal line: $fL/V_g = 0.102$. Insert: variation of $\sqrt{\rho_s/\rho_f} fL/V_g$ with $\text{Fr}\sqrt{\rho_s/\rho_f}$ for the same experiments as in the main graph. The horizontal dashed lines in the main graph and in the insert correspond respectively to values of the vertical coordinate equal to 0.102 and 0.108. The symbols correspond to the same fluids and cylinders as in Fig. 5.

view of the experiment. A setup providing a larger interval of heights over which sedimentation can be monitored will be needed to test this hypothesis.

In this problem, buoyancy forces drive the motion of the cylinders, and, at least at high Reynolds numbers, one will assume, as shown by Chow *et al.* [15] for nonconfined geometries, that the dynamics of the cylinder involves a balance between buoyancy and inertial forces. Retaining, as discussed above, L as the characteristic length, the corresponding characteristic velocity is

$$V_g = \sqrt{\frac{(\rho_s - \rho_f)gL}{\rho_f}}. \quad (9)$$

We select therefore the associated dimensionless Froude number: $\text{Fr} = V_s/V_g$ as a possible control parameter of fluttering.

Figure 6 displays the variation of Sr as a function of Fr for both types of cylinders and for all fluid solutions: there is, this time, a good collapse of the different curves and the decreasing trend is well fitted by a variation $\text{Sr} \propto 1/\text{Fr}$ (dashed line). In view of this fit, we replotted in Fig. 6 (main graph) the product $\text{Sr Fr} = f/(V_g/L)$ as a function of Fr . The curves corresponding to the different solutions and cylinders coincide well: for $\text{Fr} \leq 0.25$, the data points corresponding to the carbon cylinders are, however, slightly below those corresponding to the PMMA ones while they coincide well for $\text{Fr} \geq 0.25$. For all cylinders and solutions, the dimensionless frequency $f/(V_g/L)$ increases slightly with Fr up to $\text{Fr} \simeq 0.25$ and then becomes constant with

$$f = (0.102 \pm 0.005) \sqrt{\frac{(\rho_s - \rho_f)g}{\rho_f L}} = (0.102 \pm 0.005) \frac{V_g}{L} \quad \text{for } \text{Fr} \gtrsim 0.25. \quad (10)$$

Physically, these latter features may be understood in the perspective of a result established by Lord Rayleigh [22] for 2D plates of length L of normal tilted at an angle θ with respect to a potential flow. For $\theta \neq 0$, the pressure field is not symmetrical with respect to the centerline, and the maximum of pressure is located closer to the upstream edge of the plate. Rayleigh showed that the displacement x of the center of pressure from its location for $\theta = 0$ is $x = 3/4 L \sin \theta / (4 + \pi \cos \theta)$, which is

proportional to θL at low enough angles: the dependence on L is logical since $x = 0$ for $\theta = 0$ and L is the only characteristic length scale of the potential problem. This result was checked experimentally to remain applicable to gas flows around 3D rectangular plates [23]; it was then extended to nonconfined cylinders sedimenting in a liquid by Marchildon *et al.* [14] and Chow *et al.* [15].

In the quasistatic limit, the pressure force balances the weight of the cylinder corrected for buoyancy, the resulting restoring torque scales as $\Gamma_r \propto -[(\rho_s - \rho_f)D^2 L g](\theta L)$; Γ_r : This torque is balanced by the angular acceleration term $I d^2\theta/dt^2$ where $I \propto \rho_s L^3 D^2$ is the moment of inertia of the solid cylinder rotating around an axis perpendicular to it. This leads to a theoretical value f_{th} of the frequency of the oscillation satisfying $2\pi f_{th} = \sqrt{\Gamma_r/\theta I}$ so that

$$f_{th} \propto \sqrt{\frac{(\rho_s - \rho_f)g}{\rho_s L}} = \sqrt{\frac{\rho_f}{\rho_s}} \frac{V_g}{L}. \quad (11)$$

This expression is the same as Eq. (10) used to obtain the main graph of Fig. 6, but for the prefactor $\sqrt{\rho_s/\rho_f}$ before Fr. This difference may be due to the fact that the moment of inertia I used in the theoretical model [15] includes only the solid density ρ_s and neglects the added component of I associated to the motion of the fluid (zero entrainment); Eq. (10) corresponds instead to the case of a moment of inertia purely associated to the motion of the fluid (very strong entrainment).

We tested Eq. (11) by plotting the same data in the insert of Fig. 6 after multiplying both fL/V_g and Fr by $\sqrt{\rho_s/\rho_f}$. This time, the collapse is poorer than in the main graph for $Fr \gtrsim 0.2$ and better for $Fr \lesssim 0.2$: this suggests that one has an intermediate entrainment depending, in addition, on the value of Fr.

B. Angular and linear fluttering amplitudes

As mentioned above, both the angle θ of the axis of the cylinder with respect to the horizontal and the horizontal coordinate z_c of its center of gravity are measured continuously. After an initial overshoot, the oscillations of θ with time reach a constant amplitude θ_M and the peak to peak amplitude of those of z_c takes a value Δz_c . In their study of the case of an infinite fluid, Chow *et al.* [15] assumed that the velocity V_{osc} of the end of the cylinder scales like the sedimentation velocity V_s . Using the fact that the displacement of the end of the cylinder during an oscillation scales like $V_{osc}/f = V_s/f$ and that f may be estimated from Eq. (10), we obtain

$$\theta_M \propto \frac{V_s}{f L} = Fr. \quad (12)$$

We have therefore plotted θ_M as a function of Fr in the main graph of Fig. 7. The different data points collapse quite well, except for a few points corresponding to the lighter PMMA cylinders and to the most viscous solutions for which fluttering still occurs but which are below the common trend. In view of comparisons with the results of Chow *et al.*, we have also plotted in the insert of Fig. 7 the same data as a function of $\sqrt{\rho_s/\rho_f} Fr$ [this amounts to use in Eq. (12) the value of f computed from Eq. (11)]. The plots and, more specifically, the dispersion of the data points are similar in both graphs.

The third important parameter characterizing fluttering is the amplitude A_M of the oscillations of the center of gravity along the direction x . The values of A_M are plotted as a function of the Froude number Fr in the main graph of Fig. 8. Unlike θ_M , A_M rises sharply as Fr decreases towards the cutoff value $Fr \sim 0.07$ below which no fluttering oscillations are observed. Between ~ 0.09 and 0.07 the rising trend levels off for some of the fluid solutions and some low values of A_M are measured. Like θ_M , A_M follows roughly a common trend of variation with Fr for the solutions of lower viscosity (for PMMA cylinders) and for carbon cylinders (dashed line): this confirms that Fr is the relevant control parameter in this case. The amplitude A_M is instead, like θ_M , significantly reduced for PMMA cylinders sedimenting in the most viscous solutions; this motion corresponds to

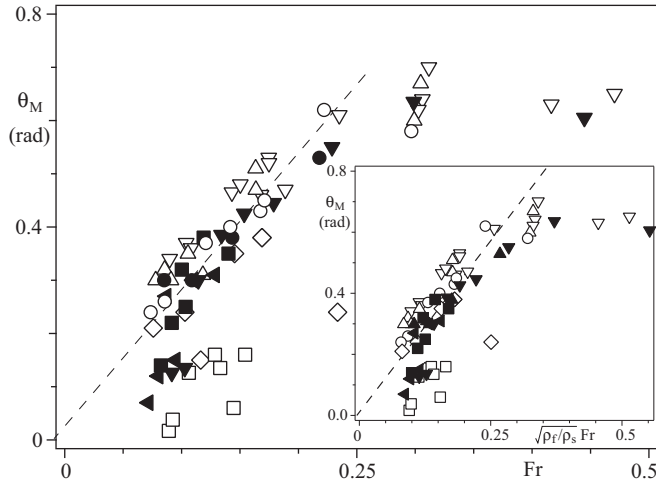


FIG. 7. Variation of the angular amplitude θ_M of the fluttering motion as a function of the Froude number Fr (main graph) and of the product $\sqrt{\rho_s/\rho_f} Fr$ (insert) for the same experiments and using the same symbols as in Fig. 5.

smaller values of the Reynolds number, which suggests that the latter needs to be taken into account in these cases.

In order to plot these same data in dimensionless coordinates, we normalized A_M by the ratio V_s/f (i.e., the mean falling distance of the cylinder during one oscillation period): like for θ_M , $A_M f/V_s$ is plotted as a function of $\sqrt{\rho_s/\rho_f} Fr$ in the insert of Fig. 8. The characteristics of this variation are qualitatively similar to that of A_M with Fr for all solutions. Plots using several other dimensionless combinations have been tested. Replacing $A_M f/V_s$ by A_M/L gives a poorer collapse; while using $(D/L)^{0.5}$ or $Fr(\rho_s/\rho_f)^{0.5}$ as suggested by the work of other authors [14,15] does not improve the collapse. We have therefore retained the present choice: the present dispersion of the data points

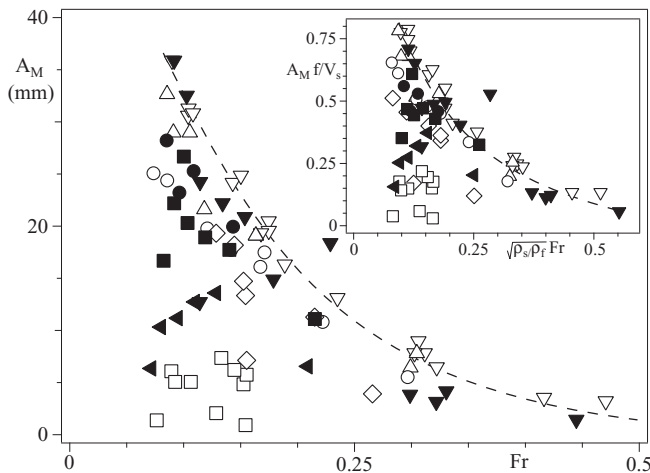


FIG. 8. Main graph: variation of the horizontal amplitude A_M of the fluttering motion of the cylinder as a function of the Froude number Fr . Insert: variation of the dimensionless amplitude $A_M f/V_s$ as a function of $\sqrt{\rho_s/\rho_f} Fr$ (insert) for the same experiments and using the same symbols as in Fig. 5.

may be due to the residual influence of the Reynolds number which is mostly important at lower values of Re .

V. DISCUSSION AND PERSPECTIVES

The present work demonstrates the decoupling between the characteristics of the average motion and of the fluttering instability for cylinders sedimenting in a Hele-Shaw cell: these differences deal, particularly, with the influence of confinement and with the key parameters of each process.

The mean velocity V_s is determined by the drag which balances the weight of the cylinders and is, in the present cell geometry, significantly larger than in the nonconfined case [15]. The Reynolds number Re_D influences strongly here V_s due to the influence of the viscous contribution to the drag which varies as $1/Re_D$. Also, the global drag coefficient C_d increases with the length of the cylinder due to the increased blockage of the flow. Instead, results from the literature in the nonconfined case indicate that C_d is smaller (for a given cylinder) and varies only slowly with the length: the sedimentation velocity is then higher, inertial drag forces are dominant, and C_d is constant with Re_D . By modeling the contributions of the viscous and inertial forces to the drag, we have also shown that the ratio of the inertial by the viscous forces follows a common increasing variation with Re_D for all cylinders and fluids studied. This ratio is equal to 1 for a relatively large Reynolds number $Re_D \simeq 40$.

Unlike for the velocity V_s , our experiments show that the key variable controlling fluttering is not Re_D but the Froude number $Fr = V_s/V_g$ (the characteristic velocity $V_g = \sqrt{\rho_s - \rho_f}gL/\rho_f$ reflects a balance between inertial and buoyancy forces). As discussed in Sec. IV A, an alternative control variable, suggested by theoretical models [14,15] is $\sqrt{\rho_s/\rho_f}Fr$. Physically, this latter definition amounts to assume that the inertia associated to the fluttering motion is determined by the solid density instead of the fluid density: this will be determined by the amount of fluid entrainment induced by the fluttering oscillations and should be larger in a confined geometry. In the present work, ρ_s/ρ_f is close to 1 so that further experiments with larger density contrasts are necessary to select the most relevant parameter; moreover, the experimental results suggest that the fluid entrainment (and therefore the correct prefactor of Fr) may depend on Fr .

The variation of the fluttering frequency with Fr is, in our experiments, very similar to that in a nonconfined geometry (unlike for the variation of V_s with Re_D). Chow *et al.* [15] reported indeed that experimental fluttering frequencies for cylinders sedimenting in a nonconfined fluid satisfied also Eq. (11) with a proportionality constant equal to 0.126. This is only 15% larger than the value 0.108 deduced from Fig. 6 (insert) by applying the same equation to our data for $\sqrt{\rho_f/\rho_s}Fr \gtrsim 0.25$: this suggests a small influence of confinement on the fluttering frequency. Another important feature is that, while there is a slight decreasing trend of fL/V_g at low Fr values $\lesssim 0.25$, there is no correlation of this variation with the value of Re_D : even data points for which viscous drag is dominant follow the common trend. A final issue is the choice of the reference variable (Fr or $\sqrt{\rho_s/\rho_f}Fr$). As mentioned above, experiments with larger density contrasts between the fluid and the cylinder are needed to investigate the relative influence of the fluid and solid densities on the fluttering frequency and the dependence of this effect on the confinement and the fluid entrainment.

The plots of the variations of the angular fluttering amplitude θ_M as a function of Fr and of $\sqrt{\rho_s/\rho_f}Fr$ both display a good collapse for almost all data points (Fig. 7). Those which do not follow this common trend correspond to PMMA cylinders and to viscous solutions (\diamond and \square symbols): then Re_D is low enough so that viscous drag forces are dominant. The angular fluttering amplitude decreases therefore at low values of Re_D while the frequency f remains constant. However, at least in the inertial regimes, the threshold of the instability is not determined by Re_D but by Fr (or equivalently $\sqrt{\rho_s/\rho_f}Fr$) as shown by the clear cutoff on the variation of θ_M at $Fr \simeq 0.07$ (or $\sqrt{\rho_s/\rho_f}Fr \simeq 0.08$). These values correspond generally to long cylinders. At large Froude numbers corresponding to the shortest cylinders ($Fr \gtrsim 0.3$), θ_M reaches a plateau value $\theta_M \simeq 0.63$ rad (i.e., $\simeq 35^\circ$) which is the same for the carbon and PMMA cylinders. The linear variation of θ_M with Fr (or $\sqrt{\rho_s/\rho_f}Fr$) predicted from Eq. (12) is actually followed (dashed line) only in the range $0.1 \lesssim Fr \lesssim 0.25$.

The variation of θ_M discussed above is also largely similar to that reported by Chow *et al.* [15] for sedimenting cylinders in a nonconfined geometry. These authors plot their experimental values of θ_M as a function of $\sqrt{\rho_s D / (\rho_f L)}$: this expression is proportional to $\sqrt{\rho_s / \rho_f} \text{Fr}$ with a constant factor (~ 1) provided Eq. (11) is valid and that the flow regime is inertial ($C_d = \text{const}$): their results can therefore be compared to the variations shown in the insert of Fig. 6. Data points corresponding to different materials of the cylinder collapse onto a same trend of variation: like in our experiments, θ_M rises initially steeply from zero above a cutoff value $\sqrt{\rho_s D / (\rho_f L)} \sim 0.25$ and then increases roughly linearly up to $\theta_M \simeq 0.87 \text{ rad}$ (50°) and levels off before rising again for $\sqrt{(D/L)(\rho_s/\rho_f)} \gtrsim 1.5$ with a transition to a tumbling regime. The initial part of the variation of the amplitude θ_M in the nonconfined case is very similar to what we observed but the tumbling regime was not observed in our experiments. Here, indeed, the largest plateau angle that was reached (35°) did not allow for a transition to tumbling.

Belmonte *et al.* [4] studied the case of a plate sedimenting between parallel walls perpendicular to it at Reynolds numbers between 3×10^3 and 4×10^4 : they reported a linear variation of $\sin \theta_M$ as a function of a Froude number with a good collapse of data corresponding to fluids of different viscosities (like for Chow *et al.*, their definition is equivalent to $\text{Fr} \sqrt{\rho_f / \rho_s}$). This variation is therefore similar to ours at low values of θ_M while they report a transition to tumbling at a Froude number of the order of 0.67. This suggests that confinement does not play a major part in this transition.

The present experiments have been performed for moderate density contrasts between the solid and the fluid: at most, the ratio ρ_s / ρ_f is of the order of 1.5; the transition towards the tumbling regime was instead generally observed for higher density contrasts between the falling object and the fluid [4,15]. This represents an additional motivation (in addition to the evaluation of the entrainment of the fluid) for performing experiments for larger density contrasts (for instance using metal cylinders): this will allow us to increase the range of values of θ_M in order to see whether the transition to tumbling is observed and whether the previous laws remain valid.

The variations with Fr of the angular and linear amplitudes (Figs. 7 and 8) are quite different, although both become zero below the cutoff Froude number $\text{Fr} \simeq 0.07$: while θ_M increases towards a plateau value as Fr increases, A_M decreases continuously to one tenth of its maximum value reached after rising sharply just above the cutoff. A qualitatively similar difference has been reported in the literature for nonconfined fluids [11,15]. Otherwise, the two amplitudes share features: in the inertial drag regime, both of their variations with Fr are independent of the viscosity and density of the fluid and of the density of the solid. Instead, when the viscous drag force become dominant ($\text{Re}_D \lesssim 40$), both amplitudes are reduced compared to the common trend in the inertial regime.

As a result and from the different models which we discussed, it seems that the cylinder diameter D influences (directly or through Re_D) the velocity V_s and the fluttering amplitude (only in the viscous drag regime) but not the frequency. This influence may be expected to rise as the ratio of D to the cell thickness becomes close to 1. This will have to be investigated by varying in a broader range the value of D (there was only a 10% difference between the two types of cylinders). Going back to our initial objective of investigating the the flow of elongated particles in porous and fractured media, the present work shows that gravity has a major influence on fluttering: the latter should therefore only be observed in vertical or near-vertical fractures and if there is a contrast between the densities of the fluid and of the particles.

ACKNOWLEDGMENTS

We thank R. Pidoux, L. Auffay and A. Aubertin for realizing and developing the experimental set up. We thank P. Ern for helpful discussions. This work has been performed in the framework of the LIA PMF-FMF (Franco-Argentinian International Associated Laboratory in the Physics and Mechanics of Fluids) and is supported by the ‘‘Investissements d’Avenir’’ Program of the LabEx PALM (ANR-10-LABX-0039-PALM).

- [1] J. C. Maxwell, On a particular case of the descent of a heavy body in a resisting medium, *Camb. Dublin Math. J.* **9**, 145 (1854).
- [2] G. Kirchhoff, Uber die Bewegung eines Rotationskorpers in einer Flussigkeit, *J. Reine Angew. Math. (Crelle)* **71**, 237 (1869).
- [3] P. Ern, F. Risso, and J. Magnaudet, Wake-induced oscillatory paths of bodies freely rising or falling in fluids, *Annu. Rev. Fluid Mech.* **44**, 97 (2012).
- [4] A. Belmonte, H. Eisenberg, and E. Moses, From Flutter to Tumble: Inertial Drag and Froude Similarity in Falling Paper, *Phys. Rev. Lett.* **81**, 345 (1998).
- [5] F. Fonseca and H. J. Herrmann, Simulation of the sedimentation of a falling oblate ellipsoid, *Physica A* **345**, 341 (2005).
- [6] S. B. Field, M. Klaus, M. G. Moore, and F. Nori, Chaotic dynamics of falling disks, *Nature (London)* **388**, 252 (1997).
- [7] L. Mahadevan, H. Aref, and S. W. Jones, Comment on "Behavior of a Falling Paper," *Phys. Rev. Lett.* **75**, 1420 (1995).
- [8] A. Andersen, U. Pesavento, and Z. J. Wang, Unsteady aerodynamics of fluttering and tumbling plates, *J. Fluid Mech.* **541**, 65 (2005).
- [9] A. Andersen, U. Pesavento, and Z. J. Wang, Analysis of transitions between fluttering, tumbling and steady descent of falling cards, *J. Fluid Mech.* **541**, 91 (2005).
- [10] P. C. Fernandes, P. Ern, F. Risso, and J. Magnaudet, On the zigzag dynamics of freely moving axisymmetric bodies, *Phys. Fluids* **17**, 098107 (2005).
- [11] P. C. Fernandes, F. Risso, P. Ern, and J. Magnaudet, Oscillatory motion and wake instability of freely rising axisymmetric bodies, *J. Fluid Mech.* **573**, 479 (2007).
- [12] M. N. Bulova, K. Nosova, D. Willberg, and J. Lassek, Benefits of the novel fiber-laden low-viscosity fluid system in fracturing low-permeability tight gas formations, in *Proceedings of the SPE Annual Technical Conference and Exhibition, San Antonio, Texas, 24–27 Sept 2006* (Society of Petroleum Engineers, 2006), paper SPE 102956.
- [13] M. N. Bulova, A. N. Cheremisin, K. E. Nosova, J. T. Lassek, and D. Willberg, Evaluation of the proppant-pack permeability in fiber-assisted hydraulic fracturing treatments for low-permeability formations, in *Proceedings of the SPE Gas Technology Symposium, Calgary, Alberta, Canada, 15–17 May 2006* (Society of Petroleum Engineers, 2006), paper SPE 100556.
- [14] E. K. Marchildon, A. Clamen, and W. H. Gauvin, Drag and oscillatory motion of freely falling cylindrical particles, *Can. J. Chem. Eng.* **42**, 178 (1964).
- [15] A. C. Chow and E. E. Adams, Prediction of drag coefficient and secondary motion of free-falling rigid cylindrical particles with and without curvature at moderate Reynolds number, *J. Hydraul. Eng.* **137**, 1406 (2011).
- [16] M. V. D'Angelo, J. P. Hulin, and H. Auradou, Oscillations and translation of a free cylinder in a confined viscous flow, *Phys. Fluids* **25**, 014102 (2013).
- [17] L. Gianorio, M. V. D'Angelo, M. Cachile, J. P. Hulin, and H. Auradou, Influence of confinement on the oscillations of a free cylinder in a viscous flow, *Phys. Fluids* **26**, 084106 (2014).
- [18] B. Semin, J. P. Hulin, and H. Auradou, Influence of flow confinement on the drag force on a static cylinder, *Phys. Fluids* **21**, 103604 (2009).
- [19] B. Semin, A. Decoene, J. P. Hulin, M. L. M. Francois, and H. Auradou, New oscillatory instability of a confined cylinder in a flow below the vortex shedding threshold, *J. Fluid Mech.* **690**, 345 (2012).
- [20] R. G. Cox, The motion of long slender bodies in a viscous fluid. Part I. General theory, *J. Fluid Mech.* **44**, 791 (1970).
- [21] A. Vakil and S. I. Green, Drag and lift coefficients of inclined finite circular cylinders at moderate Reynolds number, *Comput. Fluids* **38**, 1771 (2009).
- [22] Lord Rayleigh, LIII. On the resistance of fluids, *Philos. Mag. (5th Ser.)* **2**, 430 (1876).
- [23] A. Fage, and F. C. Johansen, On the flow of air behind an inclined flat plate of infinite span, *Proc. R. Soc. London A* **116**, 170 (1927).